Appendix A. Supplementary data

Competitive adsorption geometries for the arsenate As(V) and phosphate P(V) oxyanions on magnetite surfaces: Experiments and theory

XIAOLIANG LIANG [1, 6, 7], XIAOJU LIN [1, 7], GAOLING WEI [2, 3], LINGYA MA [1, 6, 7], HONGPING HE [1, 6, 7 *], DAVID SANTOS-CARBALLAL [4 *], JIANXI ZHU [1, 6, 7], RUNLIANG ZHU [1, 6, 7], NORA H. DE LEEUW [4, 5]

[1] CAS Key Laboratory of Mineralogy and Metallogeny/Guangdong Provincial Key Laboratory of Mineral Physics and Material Research & Development, Guangzhou Institute of Geochemistry, Chinese Academy of Sciences, Guangzhou 510640, PR China;

[2] Guangdong Key Laboratory of Integrated Agro-environmental Pollution Control and Management, Guangdong Institute of Eco-environmental Science & Technology, Guangzhou 510650, China;

[3] National-Regional Joint Engineering Research Center for Soil Pollution Control and Remediation in South China, Guangzhou 510650, China;

[4] School of Chemistry, University of Leeds, Leeds LS2 9JT, United Kingdom;

[5] Department of Earth Sciences, Utrecht University, Princetonplein 8A, 3584 CD Utrecht, The Netherlands;

[6] Institutions of Earth Science, University of Chinese Academy of Sciences, Beijing 100049, P.R. China;

[7] University of Chinese Academy of Sciences, Beijing 100049, PR China.

[*]Corresponding author. E-mail: hehp@gig.ac.cn (H.P. HE);

D.Santos-Carballal@leeds.ac.uk (D. Santos-Carballal).

TEXT. A.1. Preparation procedure of Cr-containing magnetite by a precipitation-oxidation method.

All chemicals and reagents used in this work were of analytical grade and used as received. $FeSO_4 \cdot 7H_2O$ (0.60 mol L^{-1}) and $CrCl_3 \cdot 6H_2O$ (0.30 mol L^{-1}) were dissolved in 400 mL of HCl solution. 1.0 mL hydrazine was added to prevent the oxidation of Fe^{2+} cations, and pH was low enough (< 1) to prevent Fe^{2+} oxidation and hydroxide precipitation. This solution was heated to 90-100 ℃. Equal volume of a solution containing 4.0 mol L^{-1} NaOH and 0.90 mol L^{-1} $NaNO_3$ was added dropwise (10 mL min^{-1}) into the heated iron solution and the reaction was maintained at 90 ℃ for 2 h, while stirring at a rate of 500 rpm. Then**,** the solution was cooled to room temperature. It was necessary to emphasize that during the reaction, N_2 was passed through to prevent the oxidation of Fe^{2+} by air. The particles were then separated by centrifugation at 3500 rpm for 5 min and washed with boiling distilled water, followed by an additional centrifugation. After 3-4 washings, the particles were collected and dried in a vacuum oven at 100 ℃ for 24 h. The samples was ground and passed through a 200 mesh screen. The contents of Fe and Cr were determined spectrophotometrically by the phenanthroline and 1, 5 diphenylcarbohydrazide methods. As the molar ratio of Cr/Fe was 0.287, the chemical formula of prepared Cr-containing magnetite was $Fe_{2.33}Cr_{0.67}O_4$.

TEXT. A.2. Analysis of ATR-FTIR spectra by using the 2D-COS technique.

To obtain an accurate assignment of the IR peaks for the surface complexes, the spectra were analyzed using the 2D-COS technique (Text A.2). The original spectra after baseline correction, smoothing and calculation were transferred to the 2D correlation spectra, including synchronous $\Phi(\nu_1, \nu_2)$ and asynchronous $\Psi(\nu_1, \nu_2)$ contour plots, using the 2D Shige Program ver. 1.3 (Shigeaki Morita, Kwansei-Gakuin University, 2004-2005). The intensity of the synchronous 2D correlation spectrum $\Phi(\nu_1, \nu_2)$ represents the simultaneous changes of two separate bands at ν_1 and ν_2. In the synchronous spectrum, an auto peak located at a diagonal position indicates the change of one peak intensity with time. Cross peaks located at off-diagonal positions show the response to simultaneous changes of spectral intensities observed at two different bands at ν_1 and ν_2. The intensity of an asynchronous 2D correlation spectrum $\Psi(\nu_1, \nu_2)$ represents sequential (or not simultaneous) changes of two bands at ν_1 and ν_2. The asynchronous spectrum is a powerful tool to resolve overlapped peaks and enhance the spectral resolution. In an asynchronous spectrum, only cross peaks can be found, indicating the uncorrelated response of two bands likely originating from different surface complexes. ν_1 and ν_2 change simultaneously if $\Psi(\nu_1, \nu_2)$ is zero, which indicates that they belong to the same absorption complexes. Otherwise, they display uncorrelated responses and belong to different adsorption complexes.

TEXT. A.3. Computational methods.

To simulate the interaction between the Fe_3O_4(001) surface and phosphate/arsenate oxyanions in aqueous solution, the periodic plane-wave density functional theory (DFT) method within the Vienna *ab-initio* simulation package (VASP) was employed (Kresse and Furthmüller, 1996a; Kresse and Furthmüller, 1996b; Kresse and Hafner, 1993; Kresse and Hafner, 1994). The Perdew, Burke and Ernzerhof (PBE) semi-local functional approximation was used to calculate the exchange-correlation energy (Perdew et al., 1996; Perdew et al., 1997) . The projector augmented wave (PAW) method was used to model the atomic frozen core states and their interaction with the valence levels (Fe: 4*d*5*s*, O: 2*s*2*p*, H: 1*s*, P: 3*s*3*p* and As: 4*s*4*p*) (Blöchl, 1994; Kresse and Joubert, 1999). The expansion of the Kohn-Sham (KS) valence states was calculated with a kinetic energy cut-off of 400 eV. The electronic partial occupancies were determined during geometry optimizations using the Gaussian smearing method with the width set at 0.02 eV (Mermin, 1965). Furthermore, the tetrahedron method with Blöchl corrections was used in static simulations to obtain accurate total energies as well as all the electronic and magnetic properties. Long-range dispersion interactions were modeled using the D2 semi-empirical method of Grimme (Grimme, 2006). The optimization of the structures was conducted *via* the conjugate-gradients method, which stopped when the forces on all atoms were smaller than 0.01 $eV \cdot Å^{-1}$. The Dudarev *et al.* (Dudarev et al., 1998) approach was used within the DFT+*U* methodology(Anisimov et al., 1992) to improve the description of the localized and strongly correlated Fe *d* states, which were corrected by applying the value of U_{eff} =

3.7 eV (Santos-Carballal et al., 2018; Santos-Carballal et al., 2014). All calculations were spin-polarised and the initial magnetic moments were set following a high-spin ferrimagnetic structure, *i.e.* with opposite spins in the tetrahedral and octahedral sites (Néel, 1948; Shull et al., 1951). These criteria allowed convergence of the total electronic energy within 10^{-4} eV per atom.

The Fe_3O_4(001) surface was modeled using a slab of 70.5 $Å^2$ in area, containing 56 atoms, *i.e.* 8 formula units and 7 atomic layers, and separated by a vacuum gap of 20 Å (Figure. A.2). This magnetite surface cell size with a single adsorption site is equivalent to a surface coverage of 1.42 site nm^{-2}, which is in excellent agreement with the reported value of surface site density (1-2 site nm^{-2}) (Sun et al., 1998; Tamura et al., 1993) and the detected one (3.6 site nm^{-2}, Table A.1). More details regarding the stacking of layers, a description of the surface termination and the number of frozen layers can be found elsewhere (Santos-Carballal et al., 2014). Packmol (Martínez et al., 2009) was used to pack 47 randomly positioned water molecules around the IS and outer-sphere (OS) complexes, providing a density of 1.00 g cm^{-3}. The Brillouin zone electronic integrations were performed using a $5 \times 5 \times 1$ *k*-points *Γ*-centred Monkhorst-Pack sampling grid (Monkhorst and Pack, 1976; Santos-Carballal et al., 2014). The interaction of the Fe_3O_4(001) surface with the phosphate and arsenate species was measured using the adsorption energy (E_{ads}), which was derived as

$$E_{ads} = E_{IS} - E_{OS} \quad (1)$$

where E_{IS} and E_{OS} are the energies of the IS and OS complexes. The Bader analysis

algorithm was used to partition atomic volumes and integrate charges (Henkelman et al., 2006; Sanville et al., 2007; Tang et al., 2009). The fundamental vibrational modes were calculated using the central finite difference approach (Porezag and Pederson, 1996), by allowing each ion to move by a ±0.015 Å displacement for each Cartesian coordinate. The vibrationally active atoms were defined as those belonging to the phosphate and arsenate species and also included the water molecules forming hydrogen-bonds as well as the surface ions coordinated to the solute. The coupling between the surface phonons and the vibrational frequencies of the adsorbates, all of which appeared above 500 cm^{-1}, were neglected. The outer-sphere complexes of phosphate and arsenate were modeled by placing a single solute anion in the centre of the water box filling the space between two consecutive surface slabs, corresponding to a concentration of 1.18 mol L^{-1}. The realistic concentrations of 3 to 6 orders of magnitude more dilution would require a commensurably larger and computationally prohibitive simulation cell. The acid conditions were considered in our simulations by allowing the di-protonated solute ion to dissociate upon adsorption, whereas the alkaline conditions were examined by removing one hydrogen atom from one water molecule near the mono-protonated outer-sphere species. For the inner-sphere complexes, the adsorption of the phosphate and arsenate species on the Fe_3O_4(001) surface was simulated at both acid and alkaline conditions. Different initial binding geometries including MM, BM, BB and tridentate trinuclear (TT), were taken into account. All possible binding sites were also inspected, including the protruding Fe_A atom and the Fe_B ion as well as their possible combinations.

TEXT. A.4. Simulation of outer-sphere complexes.

The outer-sphere complexes comprising the solute surrounded by water molecules are displayed in Figure. A.10. P-based anions are consistently smaller than their As-containing counterparts, as the intramolecular mean distance from the central atom to the oxygen ions differs by ~0.17 Å (Table 1), in agreement with the different radii of the central atoms (Shannon, 1976). Deprotonation leads to smaller solute size, which can be rationalized in terms of the larger number of oxygen atoms forming short double bonds with the pnictogen atom. However, in this study, the degree of protonation of the solute does not noticeably affect the single and double bond distances (Table 1). The radial distribution function clearly shows three solvation shells around the solute anion, which are formed at 3.3 − 4.0 Å, 4.5 − 4.8 Å and 5.8 − 6.0 Å from the central atom (Figure. A.11). Although the average of the six bond angles centered on *X*, where *X* represents As or P , is equal to 109.5 °, the general order of increasing values is ∠(O−*X*−O) < ∠(O−*X*=O) < ∠(O=*X*=O), with the exception of $HAsO_4$, where ∠(O−As=O) ≈ ∠(O=As=O) (Table 1). The repulsion between the two oxygen atoms, which is larger in O=*X*=O than in O−*X*−O explains qualitatively the trend that we found for the values of the bond angles. The mean bond angle involving the hydrogen atom of H_2PO_4 is 6.18 ° smaller than for HPO_4, but our calculations predict only a negligible difference between the mono- and di-protonated arsenic species. As expected, the Bader charges of the solute ions are underestimated by ~17% with respect to their formal charges, which increases to ~23% with the pH value (Table 2). For the outer-sphere complexes under alkaline conditions, a charge of

approximately −0.66 e^- was calculated for the OH groups (Table 2), which prefer to coordinate the protruding Fe_A ion at 1.92 and 1.95 Å for $HAsO_4^{2-}$ and HPO_4^{2-}, respectively (Figure. A.10).

The wavenumbers of the fundamental vibrational modes for the arsenate and phosphate OS complexes under both acid and alkaline conditions were also calculated, which are displayed in Table 3 alongside their molecular point groups. Given the high mass ratio between As, P or O and H, which lies between 74 and 16, the six fundamental vibrations involving the light H atoms are faster and can be considered decoupled from the rest of the normal modes of the oxyanions. Under acid conditions, the di-protonated arsenate ($H_2AsO_4^-$) and phosphate ($H_2PO_4^-$) ions are the dominant species with C_{2v} symmetry and 15 fundamental vibrational modes. The expected modes are 6 vibrations involving the H atoms and 9 modes for the rest of the molecule. Alkaline pH values lead to the deprotonation of the outer-sphere complexes, thus increasing their symmetry to the C_{3v} molecular point group, with a reduction to 3 singly degenerate vibrations for the H atom. The vibrational modes of the hydrogens, which are difficult to measure experimentally due to exchange with the solvent, are the stretching $\nu(X\text{O}-\text{H})$, bending $\delta(X\text{OH})$ and wagging $\omega(X\text{OH})$, in decreasing order of their typical wavenumbers. The remaining vibrations are 4 stretching and 5 angle vibrational modes originating solely from the central atom of the adsorbate and its surrounding oxygens. For the $X{=}O_2$ and $X{-}(OH)_2$ groups of the di-protonated C_{2v} species, there are two singly degenerate asymmetric vibrations at high wavenumber and two softer singly degenerate symmetric stretching modes. The mono-protonated

C_{3v} species have one singly degenerate symmetric and one doubly degenerate asymmetric stretching modes for the $X{=}O_3$ group plus one singly degenerate stretching for the $X{-}$OH group. However, the interaction with environmental species, such as water solvent, breaks the adsorbate symmetry, making all fundamental modes effectively non-degenerate. The 5 fundamental angle modes for the adsorbate molecules appear significantly mixed below 600 cm^{-1} and thus we do not consider them for further analysis. Generally, most of the fundamental vibrational modes for As-containing anions are red-shifted with respect to their phosphate counterparts, in excellent agreement with the ATR-FTIR experiments (Table 3). The only exceptions are the stretching ν(PO−H) and bending δ(POH) for HPO_4^{2-} and $H_2PO_4^-$, respectively, which appear at higher wavenumbers than for the iso-structural As-based molecules. However, taking into account that the bending δ(POH) is 1245.01 cm^{-1} for $H_2PO_4^-$ at acid pH (Table 3), which compares closely with the experimental value of 1240 cm^{-1} (Figure. A.6), we are confident of the predictive accuracy and consistency of our approximate vibrational modes.

TEXT. A.5. 2D-COS analysis of ATR-FTIR spectra.

To further investigate the adsorption configuration of arsenate and phosphate on the magnetite surfaces, 2D-COS was used to analyze the time-dependent spectra at pH = 4.0, 7.0 and 9.0. The synchronous spectra (Figures. A.6a-c) of arsenate revealed that the intensity of the auto-peak at 855 cm^{-1} obviously increased as adsorption proceeded. Based on the asynchronous spectra (Figures. A.6d-f) and correlation (Table A.2), the band at 855 cm^{-1} was asynchronous with those at 870, 830 and 805 cm^{-1}, which are attributed to different adsorption complexes according to Noda's rule (Noda, 1990).

For the synchronous 2D-COS analysis of phosphate, the auto-peaks (Figures. A.10a-c) at 1028 cm^{-1} (low pH) and 1050 cm^{-1} (high pH) increased their intensity as adsorption proceeded, while the asynchronous spectra exhibited cross-peaks at 1108, 1075, 1050, 1028, 1000, 965 and 870 cm^{-1} (Figures. A.10d-f). Based on the correlation (Table A.3) of the asynchronous cross-peaks at 1075, 1028 and 965 cm^{-1} and at 1108, 1050, 1000 and 870 (υ_1) cm^{-1}, the two sets were assigned to different IS complexes. Both complexes had three ν_3 vibrations, indicating a C_{2v} symmetry or lower. Through the deconvolution of the spectra (Figure. 1b) and the calculation of its sub-spectral area (Figure. 2b), the contribution of each predominant adsorbed phosphate complex was calculated at acid and alkaline pH (Figure. 2b).

TABLE A.1. Surface properties of Cr-containing magnetite.

Lattice parameter a_0/Å	Crystal size/nm	Specific surface area (m^2g^{-1})	Surface site density/site nm^{-2}	pH_{pzc}
8.384	26	112	3.6	6.8

TABLE A.2. A synchronous relationship of peaks on the asynchronous spectra of arsenate adsorbed on magnetite surface.

Wavenumber/cm^{-1}	870	855	830	790
870		√		
855	√		√	√
830		√		
790		√		

√: the asynchronous correlation of cross peak $\psi(\upsilon_1, \upsilon_2)$.

TABLE A.3. A synchronous relationship of peaks on the asynchronous spectra of phosphate adsorbed on magnetite surface.

Wavenumber/cm^{-1}	1108	1075	1050	1028	1000	965	870
1108		√		√		√	
1075	√		√				
1050		√		√		√	
1028	√		√		√		
1000				√		√	
965	√		√		√		√
870						√	

√: the asynchronous correlation of cross peak $\psi(\upsilon_1, \upsilon_2)$.

Figure. A.1. XRD pattern of Cr-containing magnetite.

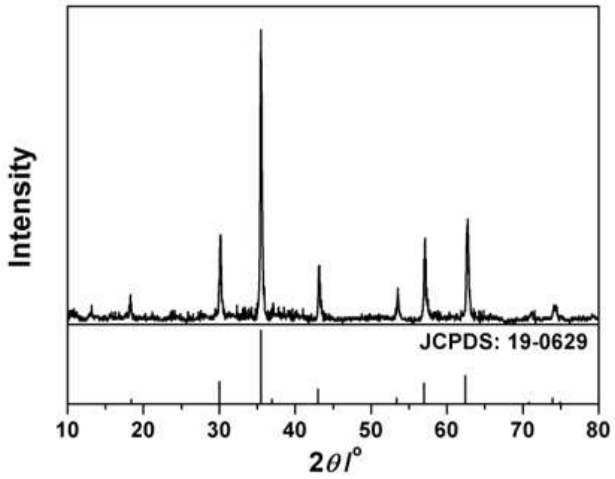

Power X-ray diffraction (PXRD) were recorded between 10 °and 80 °(2θ) at a step of 1 °min^{-1} using a Bruker D8 advance diffractometer with Cu *K*α radiation (40 kV and 40 mA). The XRD pattern of Cr containing magnetite well corresponds to the standard card of magnetite (JCPDS: 19-0629), confirming that the prepared sample has spinel structure.

Figure. A.2. (a) Top and (b) side view of the simulation slab for the $Fe_3O_4(001)$ surface.

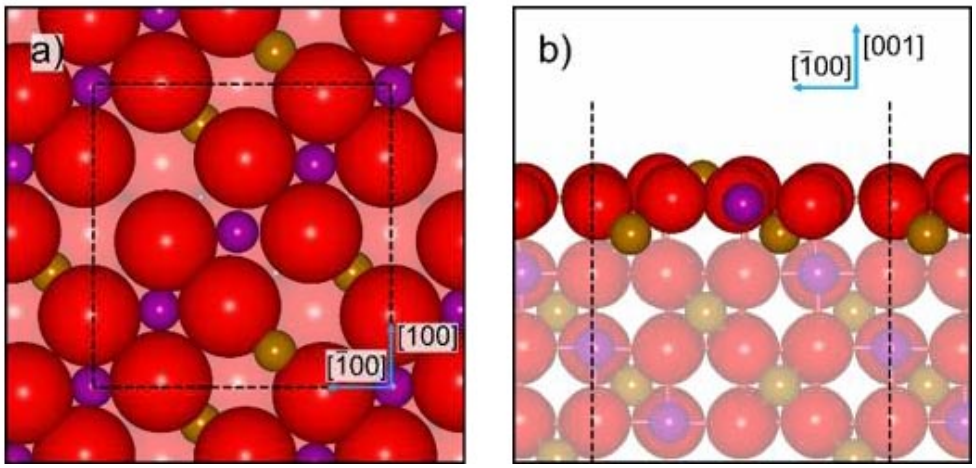

Layers containing atoms with dangling bonds are highlighted. Tetrahedral Fe_A atoms are in orange, octahedral Fe_B atoms are in violet and O atoms are in red Dashed lines mark the limits of the computational cell. Crystallographic directions are indicated.

Figure. A.3. Spectrum of arsenate adsorbed on magnetite at different pH (arsenate concentration: 100 μmol L^{-1}, range of pH: 4-9).

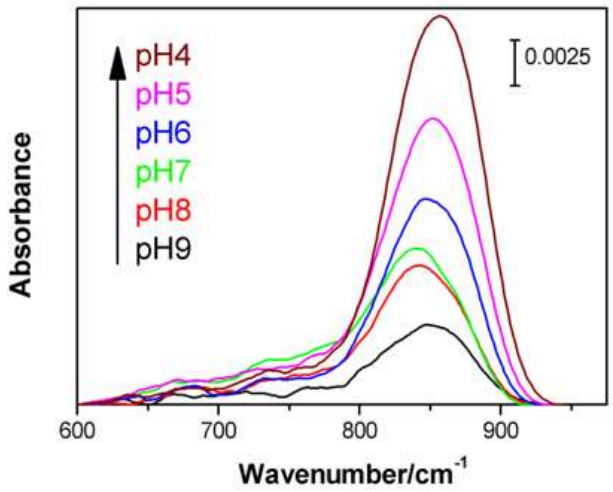

The adsorption of arsenate on magnetite in pH range of 4-9 is studied by *in situ* ATR-FTIR, as the intensity of the band is proportional to the content of arsenate species adsorbed on magnetite surface. With the decrease of pH, the arsenate adsorption is obviously increased (Figure. A.3).

Figure. A.4. Spectrum of free arsenate oxyanions recorded at different pH.

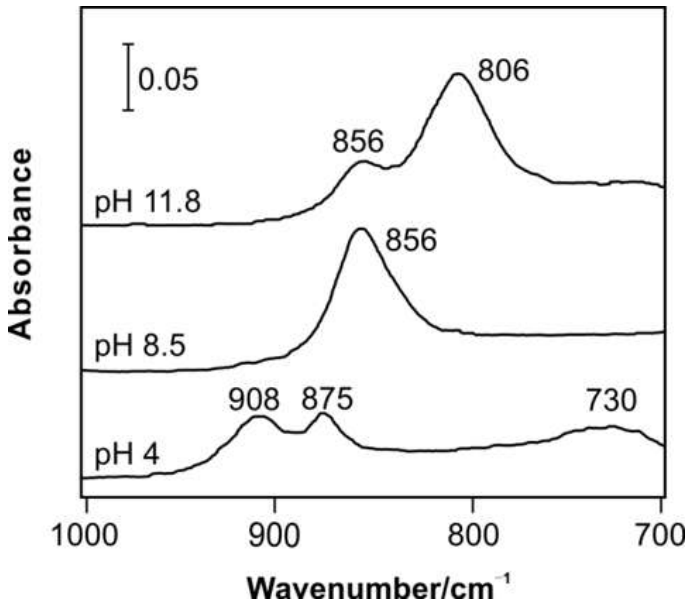

Based on the pK_{a1} (2.2), pK_{a2} (6.7) and pK_{a3} (11.2) values of arsenate (Mohan and Pittman, 2007), the predominant aqueous species at pH = 3.0 was $H_2AsO_4^-$, while $HAsO_4^{2-}$ was dominant at pH = 9 and AsO_4^{3-} together with $HAsO_4^{2-}$ dominated at pH = 12. The differences in protonation and thus symmetry of the above aqueous arsenate species were well-illustrated by IR spectra (Figure. A.4) (Carabante et al., 2009). At pH = 4, three bands appeared at 908, 878 and 738 cm^{-1}, assigned to the As-O asymmetrical stretching (υ_3) of the $H_2AsO_4^-$ aqueous species with C_{2v} symmetry. The spectrum recorded at pH = 8.5 for $HAsO_4^{2-}$ with C_{3v} symmetry showed a broad signal at 858 cm^{-1} composed of two υ_3 bands overlapped at 865 and 846 cm^{-1}, due to the stretching of As-O (Myneni et al., 1998). At pH = 11.8, the main signal at 802 cm^{-1} was related to the υ_3 band of AsO_4^{3-} with tetrahedral symmetry (T_d), which was accompanied by a weak band at 858 cm^{-1} originating from $HAsO_4^{2-}$. Thus, with the reduction of symmetry from T_d to C_{3v} and subsequently to C_{2v} or C_1, the υ_3 vibrational mode was split from a single band into two and then three bands.

Figure. A.5. Spectral variation of arsenate adsorbed on Cr containing magnetite during its desorption by NaCl solution (NaCl concentration: 100 mmol L^{-1}, pH: 4.0)..

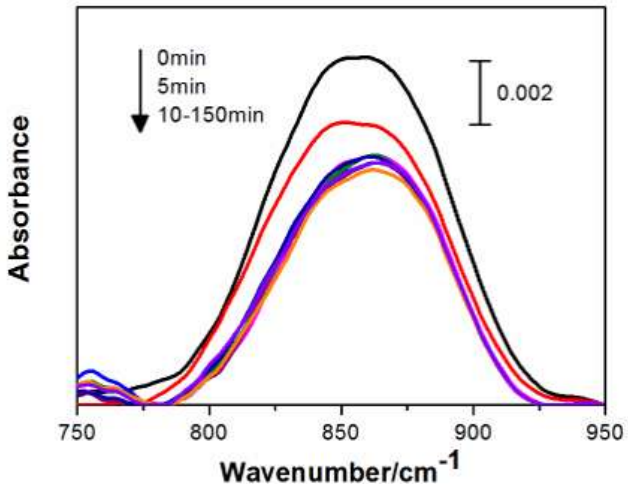

Once the arsenate solution in ZnSe cell is replaced by NaCl solution at pH 4.0, the band quickly decreases in intensity to some extent, but then keeps stable even after long period of desorption.

Figure. A.6. The two-dimensional synchronous (a-c) and asynchronous spectra (d-f) of arsenate adsorption on magnetite at pH 4.0 (a, d), 7.0 (b, e) and 9.0 (c, f).

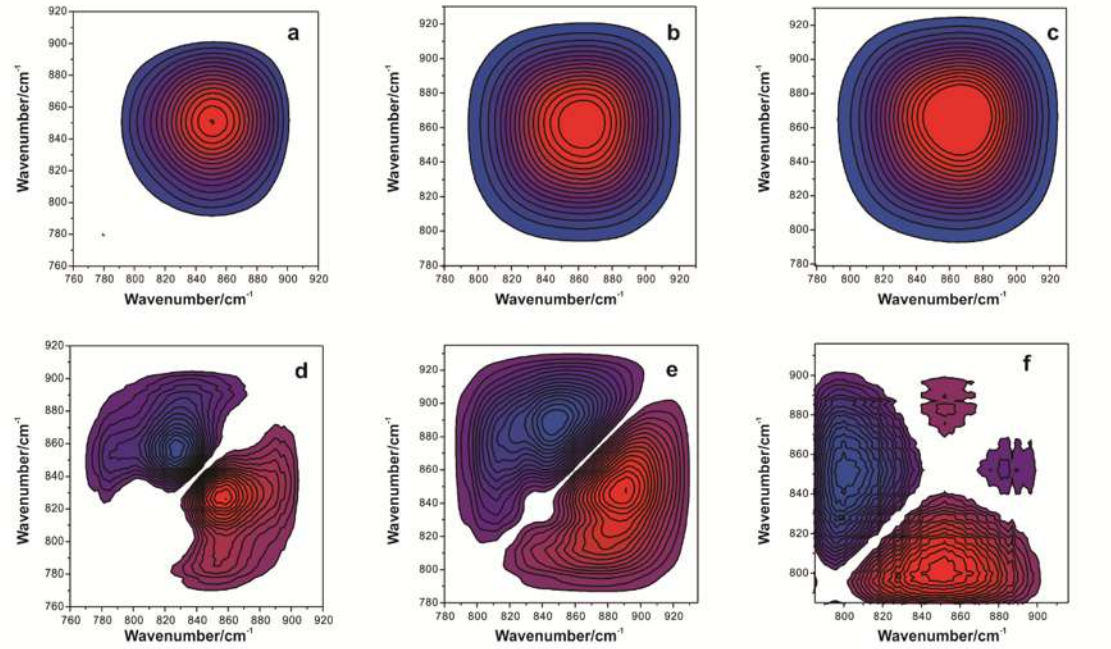

Figure. A.7. Spectrum of phosphate adsorbed on Cr containing magnetite at different pH (phosphate concentration: 100 μmol L^{-1}, range of pH: 4-9).

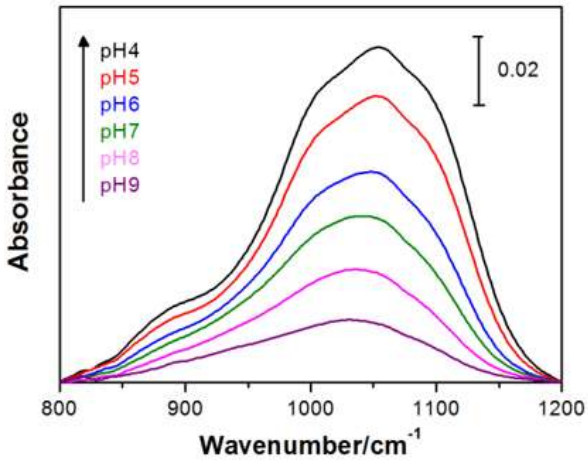

The adsorption of phosphate on magnetite in pH range of 4-9 is studied by *in situ* ATR-FTIR, as the intensity of the band is proportional to the content of phosphate species adsorbed on magnetite surface. With the decrease of pH, the phosphate adsorption is obviously increased (Figure. A.7).

Figure. A.8. Spectrum of free phosphate oxyanions recorded at different pH.

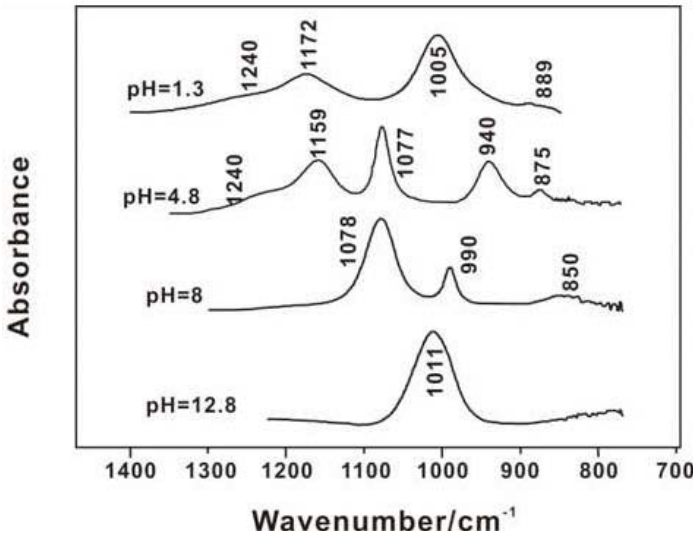

The pKa_1, pKa_2 and pKa_3 of phosphate were 2.2, 7.2 and 12.3, respectively. At pH = 12.8, the predominant aqueous species of phosphate was fully deprotonated (PO_4^{3-}) with T_d symmetry, which showed a single υ_3 vibration at 1006 cm^{-1} (Figure. A.8). At pH = 8, the main aqueous species became monoprotonated (HPO_4^{2-}) with C_{3v} symmetry, which was characterized by an active υ_1 band at 855 cm^{-1} and one υ_3 vibration, split into two bands at 1078 and 990 cm^{-1}. At pH = 4.8, the di-protonated species ($H_2PO_4^-$) with C_{2v} symmetry dominated, showing three υ_3 bands at 1159, 1077 and 940 cm^{-1} and one υ_1 mode at 875 cm^{-1}. Further reduction of the pH value to 1.3, led to H_3PO_4 with C_{3v} symmetry to become the predominant species, producing two separate υ_3 bands at 1172 and 1005 cm^{-1}, and one υ_1 band at 889 cm^{-1}. For the two highest protonated $H_2PO_4^-$ and H_3PO_4 aqueous species, the spectra displayed a broad band at 1240 cm^{-1}, which was attributed to the bending of δ(POH) (Elzinga and Sparks, 2007).

Figure. A.9. Spectral variation of phosphate adsorbed on Cr containing magnetite during its desorption by NaCl solution (NaCl concentration: 100 mmol L^{-1}, pH: 4.0).

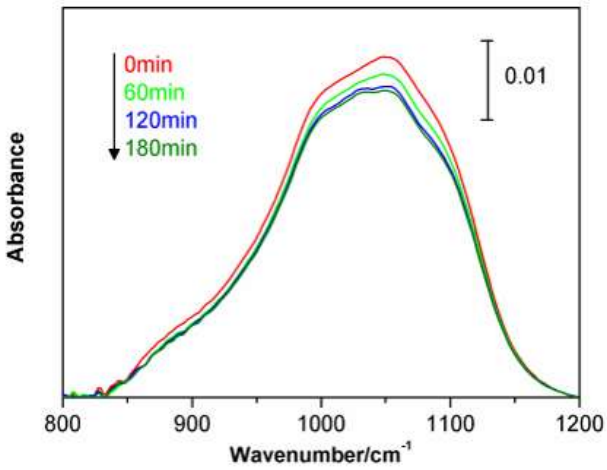

Although the phosphate solution in ZnSe cell was replaced by NaCl solution at pH 4.0 for a long period of desorption, the band just slightly decreased in intensity.

Figure. A.10. The two-dimensional synchronous (a-c) and asynchronous spectra (d-f) of phosphate adsorption on Cr-containing magnetite at pH 4.0 (a, d), 6.0 (b, e) and 9.0 (c, f).

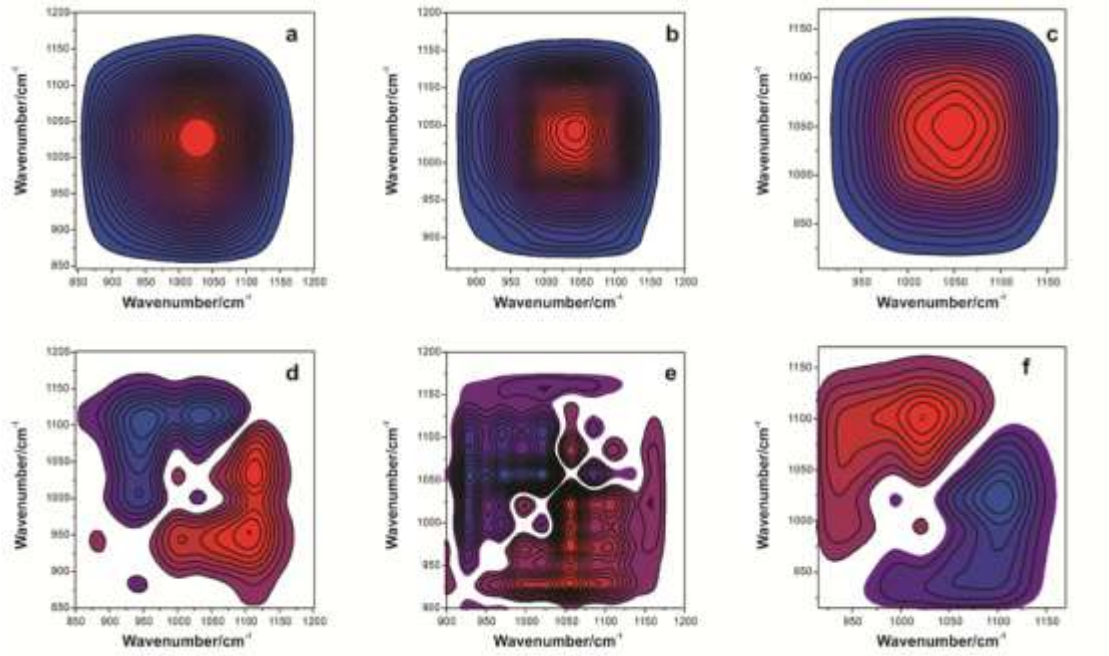

Figure. A.11. Schematic representation of the aqueous outer-sphere species (a) $H_2PO_4^-$, (b) HPO_4^{2-}, (c) H_2AsO^{4-}, and (d) $HAsO_4^{2-}$.

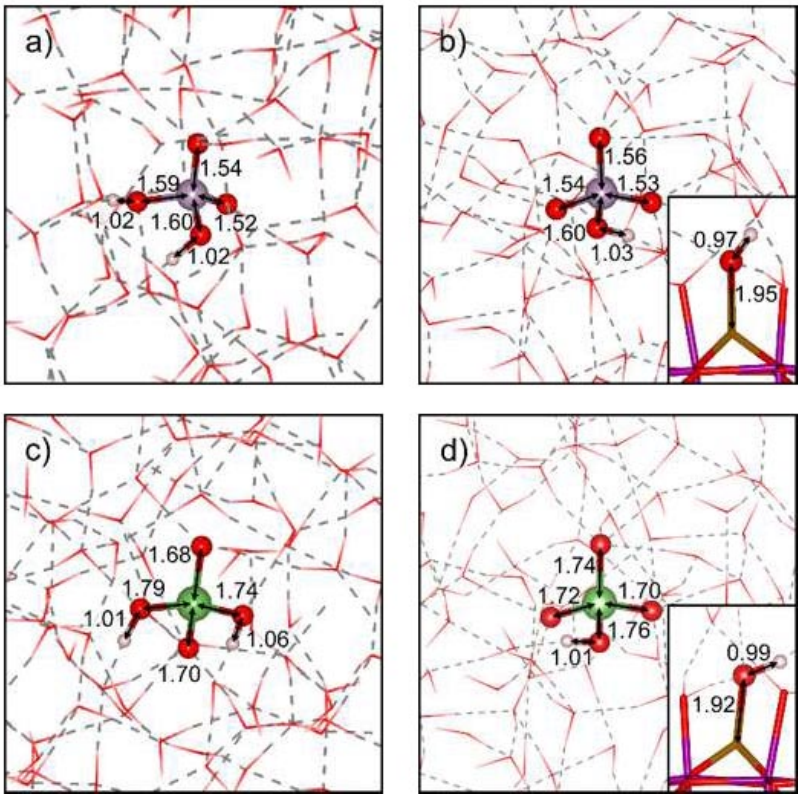

Di- and mono-protonated solute anions are under acid and alkaline conditions, respectively. Tetrahedral Fe_A atoms are in orange, octahedral Fe_B atoms are in violet, O atoms are in red, P atoms are in blue, As atoms are in green and H atoms are in pink. Surface atoms are represented as sticks, water solvent molecules are represented as wireframe and the solute molecules are represented as balls-and-sticks. Light and dark dashed lines mark hydrogen bonds and the limits of the computational cell, respectively. The double arrows indicate interatomic distances in Å.

Figure. A.12. Radial distribution function [g(r)] plots for (a) $H_2PO_4^-$, (b) HPO_4^{2-}, (c) $H_2AsO_4^-$, and (d) $HAsO_4^{2-}$.

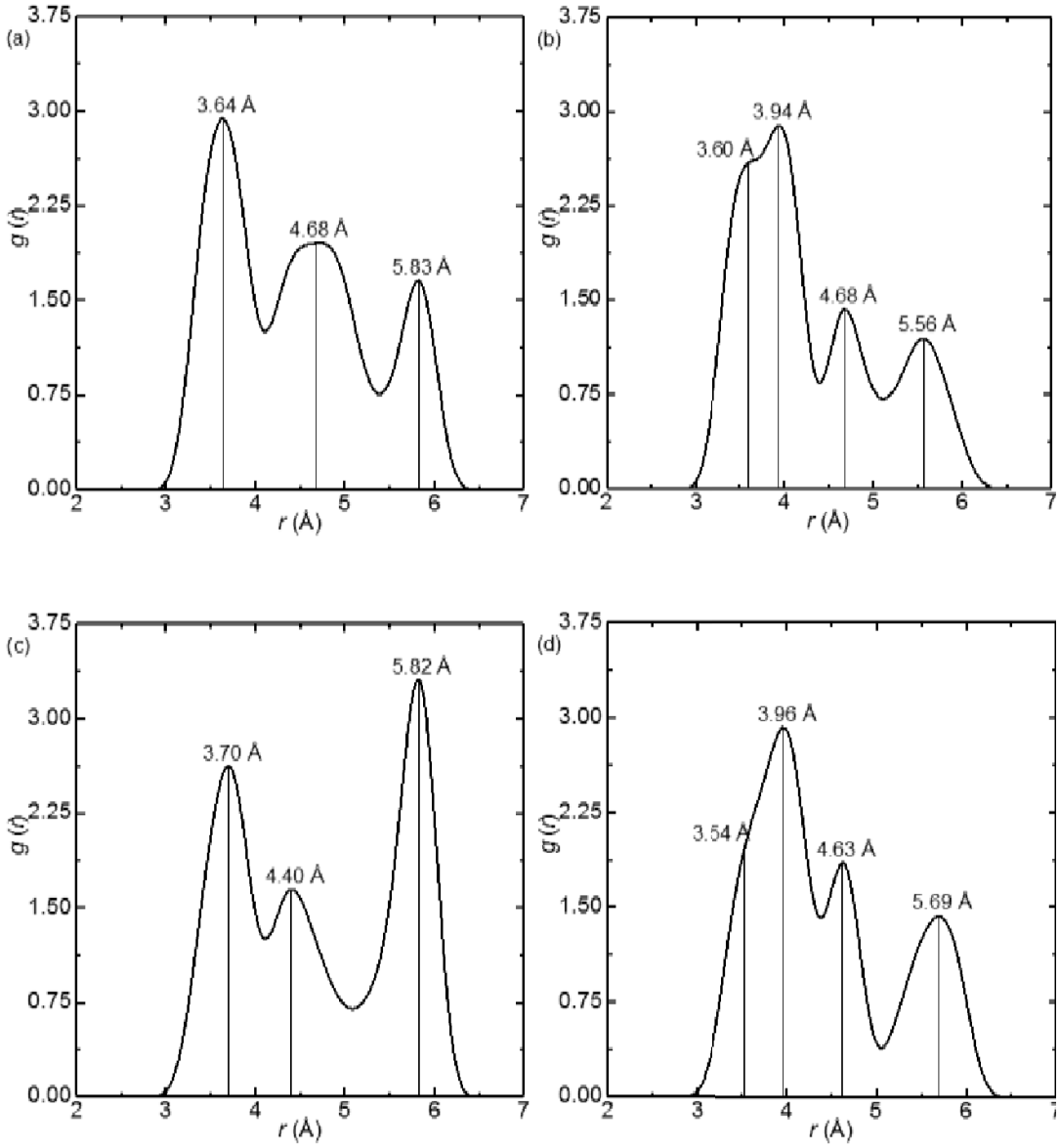

Di- and mono-protonated solute anions are under acid and alkaline conditions, respectively. The radii are measured from the P or As solute central atom to the O of the water molecules. The radial distribution function was integrated using a width for the spherical shells of 0.3 Å.

References

Anisimov, V.I., Korotin, M.A., Zaanen, J., and Andersen, O.K. (1992) Spin bags, polarons, and impurity potentials in $La_{2-x}Sr_xCuO_4$ from first principles. Physical Review Letters, 68(3), 345-348.

Blöchl, P.E. (1994) Projector augmented-wave method. Physical Review B, 50(24), 17953-17979.

Carabante, I., Grahn, M., Holmgren, A., Kumpiene, J., and Hedlund, J. (2009) Adsorption of As (V) on iron oxide nanoparticle films studied by in situ ATR-FTIR spectroscopy. Colloids and Surfaces a-Physicochemical and Engineering Aspects, 346(1-3), 106-113.

Dudarev, S.L., Botton, G.A., Savrasov, S.Y., Humphreys, C.J., and Sutton, A.P. (1998) Electron-energy-loss spectra and the structural stability of nickel oxide: An LSDA+U study. Physical Review B, 57(3), 1505-1509.

Elzinga, E.J., and Sparks, D.L. (2007) Phosphate adsorption onto hematite: An in situ ATR-FTIR investigation of the effects of pH and loading level on the mode of phosphate surface complexation. Journal of Colloid and Interface Science, 308(1), 53-70.

Grimme, S. (2006) Semiempirical GGA-type density functional constructed with a long-range dispersion correction. Journal of Computational Chemistry, 27(15), 1787-1799.

Henkelman, G., Arnaldsson, A., and Jónsson, H. (2006) A fast and robust algorithm for Bader decomposition of charge density. Computational Materials Science,

36(3), 354-360.

Kresse, G., and Furthmüller, J. (1996a) Efficiency of ab-initio total energy calculations for metals and semiconductors using a plane-wave basis set. Computational Materials Science, 6(1), 15-50.

-. (1996b) Efficient iterative schemes for ab initio total-energy calculations using a plane-wave basis set. Physical Review B, 54(16), 11169-11186.

Kresse, G., and Hafner, J. (1993) Ab initio molecular dynamics for liquid metals. Physical Review B, 47(1), 558-561.

-. (1994) Ab initio molecular-dynamics simulation of the liquid-metal-amorphous-semiconductor transition in germanium. Physical Review B, 49(20), 14251-14269.

Kresse, G., and Joubert, D. (1999) From ultrasoft pseudopotentials to the projector augmented-wave method. Physical Review B, 59(3), 1758-1775.

Martínez, L., Andrade, R., Birgin, E.G., and Martínez, J.M. (2009) PACKMOL: A package for building initial configurations for molecular dynamics simulations. Journal of Computational Chemistry, 30(13), 2157-2164.

Mermin, N.D. (1965) Thermal Properties of the Inhomogeneous Electron Gas. Physical Review, 137(5A), A1441-A1443.

Mohan, D., and Pittman, C.U. (2007) Arsenic removal from water/wastewater using adsorbents - A critical review. Journal of Hazardous Materials, 142(1-2), 1-53.

Monkhorst, H.J., and Pack, J.D. (1976) Special points for Brillouin-zone integrations. Physical Review B, 13(12), 5188-5192.

Myneni, S.C.B., Traina, S.J., Waychunas, G.A., and Logan, T.J. (1998) Experimental and theoretical vibrational spectroscopic evaluation of arsenate coordination in aqueous solutions, solids, and at mineral-water interfaces. Geochimica Et Cosmochimica Acta, 62(19-20), 3285-3300.

Néel, M.L. (1948) Propriétés magnétiques des ferrites; ferrimagnétisme et antiferromagnétisme. Annales de Physique, 12, p. 137-198.

Noda, I. (1990) Two-dimensional infrared (2D IR) spectroscopy: theory and applications. Applied Spectroscopy, 44(4), 550-561.

Perdew, J.P., Burke, K., and Ernzerhof, M. (1996) Generalized Gradient Approximation Made Simple. Physical Review Letters, 77(18), 3865-3868.

-. (1997) Generalized Gradient Approximation Made Simple [Phys. Rev. Lett. 77, 3865 (1996)]. Physical Review Letters, 78(7), 1396-1396.

Porezag, D., and Pederson, M.R. (1996) Infrared intensities and Raman-scattering activities within density-functional theory. Physical Review B, 54(11), 7830-7836.

Santos-Carballal, D., Roldan, A., Dzade Nelson, Y., and de Leeuw Nora, H. (2018) Reactivity of CO_2 on the surfaces of magnetite (Fe_3O_4), greigite (Fe_3S_4) and mackinawite (FeS). Philosophical Transactions of the Royal Society A: Mathematical, Physical and Engineering Sciences, 376(2110), 20170065.

Santos-Carballal, D., Roldan, A., Grau-Crespo, R., and de Leeuw, N.H. (2014) A DFT study of the structures, stabilities and redox behaviour of the major surfaces of magnetite Fe_3O_4. Physical Chemistry Chemical Physics, 16(39), 21082-21097.

Sanville, E., Kenny, S.D., Smith, R., and Henkelman, G. (2007) Improved grid-based algorithm for Bader charge allocation. Journal of Computational Chemistry, 28(5), 899-908.

Shannon, R. (1976) Acta Crystallogr., Sect. A: Cryst. Phys., Diffr., Theor. Gen. Crystallogr.

Shull, C.G., Wollan, E.O., and Koehler, W.C. (1951) Neutron Scattering and Polarization by Ferromagnetic Materials. Physical Review, 84(5), 912-921.

Tang, W., Sanville, E., and Henkelman, G. (2009) A grid-based Bader analysis algorithm without lattice bias. Journal of Physics: Condensed Matter, 21(8), 084204.